Supplementary Information

SP94-Targeted Triblock Co-Polymer Nanoparticle Delivers Thymidine Kinase-p53-Nitroreductase Triple Therapeutic Gene and Restores Anticancer Function against Hepatocellular Carcinoma *in vivo*

Uday K. Sukumar, Jagadesh Chandra Bose Rajendran, Sanjiv S. Gambhir, Tarik F. Massoud and Ramasamy Paulmurugan*

Department of Radiology, Molecular Imaging Program at Stanford (MIPS), Stanford University School of Medicine, 3155 Porter Drive, Palo Alto, CA 94305, USA.

Table of Contents

Supplementary Materials and Methods

Materials

Carboxy terminal Poly (lactic-co-glycolic acid)/-polyethylene glycol acid conjugate polymer was purchased from Poly SciTech (West Lafayette, IN). Linear polyethyleneimine (LPEI, Mw: 10,000) and dextrose were purchased from Sigma-Aldrich (St. Louis, MO, USA). Poly(ethylene glycol) bis(amine) (MW 3,400) was purchased from Laysan Bio, Inc. (Arab, Al, USA). Lipofectamine 2000, fetal bovine serum (FBS), cell culture media, streptomycin and penicillin were purchased from Thermo Fisher Scientific (Waltham, MA, USA). DNA gel extraction and plasmid extraction kits were procured from Epoch Life Sciences (Sugar Land, TX). CytoCy5S was obtained from GE Healthcare. The prodrugs ganciclovir (GCV) and 5-(aziridin-1-yl)-2, 4-dinitrobenzamide (CB1954) were purchased from Sigma-Aldrich (St Louis, MO, USA). β-mercaptoethanol was purchased form Bio-Rad. A 4-12% SDS-polyacrylamide gel electrophoresis gradient gel from Invitrogen was used for Immunoblot analysis, and 0.2 mm pore size nitrocellulose membrane was purchased from Schleicher & Schuell (Keene, NH, USA). The primary antibodies and IgG anti-rabbit secondary antibody were acquired from Cell Signaling Technology (Danvers, MA, USA). Pierce ECL Western Blotting Substrate was obtained from Thermo Fisher Scientific, USA. Cell culture plates were purchased from BD Diagnostic Systems (Sparks, MD, USA). HepG2 (Human hepatocellular carcinoma [p53 wild type]) and Hep3B (Human hepatocellular carcinoma [p53 mutant]) cell lines was purchased from American Type Culture Collection (Manassas, VA, USA). Plasmid extraction, DNA gel extraction, and genomic DNA extraction kits were purchased from Epoch Life Sciences (Sugar Land, TX).

Methods

Cell culture. HepG2 and Hep3B cells were cultured in Dulbecco's Modified Eagle's Medium supplemented with 10% FBS, 100 U/mL penicillin, and 0.1% streptomycin in a 37 °C incubator with 5% CO_2 and 95% air. The cells were tested for mycoplasma contamination by MycoAlert kit from Lonza (Allendale, NJ) and maintained at optimum culture conditions as per ATCC guidelines.

Plasmid constructs and DNA isolation. The plasmid vectors used in this study, expressing bacterial nitroreductase gene (NTR2), mutant HSV1-thymidine kinase-nitroreductase (HSV1sr39TK–NTR), thymidine kinase-p53-nitroreductase (HSV1sr39TK-p53-NTR) fusion, and Fluc-EGFP fusion constructs were from our plasmid bank (Cellular Pathway Imaging Laboratory, Stanford). All the expression cassettes were in pcDNA-3.1 backbone with CMV or Ubiquitin promoter driving expression.

Synthesis of SP94 conjugated PLGA-PEG. Carboxy-terminated PLGA-PEG (10 mg) conjugate polymer was dispersed in 1 mL dichloromethane (DCM) and supplemented with 2.4 mg (21 μmol) of NHS (N-hydroxysuccinamide, Sigma), and 4.1 mg (21 μmol) of EDC (1-Ethyl-3-(3-dimethylaminopropyl)carbodiimide, Sigma). The pH was adjusted to 3.5, and the mixture incubated for 6 h at 4 °C with gentle stirring. A total of 8.5 mg of NHS activated PLGA-PEG was dissolved in 0.25 mL of DCM and then added to 0.25 mL of DMSO (Sigma-Aldrich) containing 3.1 mg of SP94 peptide/scrambled peptide. The mixture was supplemented with 0.011 mL of triethylamine to catalyze the reaction and then stirred for 72 h at room temperature. The stoichiometric molar ratio of peptide and NHS-PEG-COOH was 1.1:1. The PLGA-PEG-peptide conjugates were purified by dialysis with a 2 kDa cut-off membrane, and were then dried through lyophilization. The presence of the peptides was confirmed by FTIR and MALDI-TOF mass spectrometry, as reported previously [1].

Characterization of PLGA-PEG-PEI conjugated polymer. The effective conjugation of the amine group of PEI to the terminal COOH group of PLGA-PEG was assessed by Fourier transform infrared (FTIR) analysis. The conjugated polymer was freeze-dried and blended with KBr (99+% purity, IR grade) and then compressed into KBr pellets (by applying a pressure of 300 kg cm^{-2}) in order to increase translucency for FTIR analysis. The samples were scanned in the range 4000−5000 cm^{-1} using a Bruker Vertex 70 FTIR spectrometer. Apart from the conjugated polymer, FTIR spectra of precursor polymers, i.e. PLGA-PEG-COOH and PEI, were also acquired for unambiguous interpretation of peaks. The efficiency of conjugation chemistry was further cross-validated by Nuclear Magnetic Resonance (NMR) spectroscopy by analysis of samples in a Varian 400 NMR spectrometer. 1H NMR spectra of conjugated polymers and the precursors

dissolved in deuterated chloroform ($CDCl_3$) were acquired at 400 MHz at room temperature and the results were processed using a VNMR software console.

PLGA-PEG-PEI Nanoparticle characterization. PLGA-PEG-PEI nanoparticles and PLGA-PEG-PEI/DNA complexes mean hydrodynamic diameters were measured by dynamic light scattering (DLS) in a Malvern Zetasizer Nano Z system. The zeta-potential (surface charge) of the polymers and polyplexes were determined at 25 °C with a scattering angle of 90°. Samples were prepared in PBS and diluted with deionized water to ensure that the measurements are performed under conditions of low ionic strength where the surface charge of the particles can be measured accurately. The particle size and morphology of the PLGA-PEG nanoparticles, PLGA-PEG-PEI nanoparticles, plasmid-loaded PLGA-PEG-PEI, and SP94/scrambled modified and PLGA-PEG-PEI nanoparticles or plasmid complexes were characterized using a Scanning electron microscope (Sigma FE-SEM, Zeiss, NY, USA).

Synthesis of SP94/scrambled-SP94 and PEI grafted PLGA-PEG nanoparticles. PLGA-PEG-PEI (NHS activated) and SP94/scrambled-peptide conjugated PLGA-PEG-PEI nanoparticles loaded with suicide genes were formulated using water-in-oil-in-water (w/o/w) double emulsion method [2]. The carboxy-terminated PEGylated PLGA (4 mg), PEGylated PLGA (NHS activated) (4 mg) and SP94-conjugated PLGA-PEG (2 mg/mL) were dissolved in DCM in a 20 mL scintillation vial to form a homogenous solution. Subsequently, 0.25 mL of ultrapure water was added dropwise into the PLGA-PEG solution under constant stirring. Immediately after addition of aqueous phase the mixture was subjected to probe sonication at 40% amplitude for 1 min in an ice bath to form the first emulsion. The resultant emulsion was added drop wise into 4 mL of a second aqueous phase with PEI (1 mg) and 1% PVA (w/v) and again subjected to sonication for 1 min at 40% amplitude under ice cold conditions to form the second emulsion. The w/o/w emulsion of PLGA-PEG-PEI nanoparticles were further stabilized by stirring for 6 h at room temperature. After the completion of the incubation period, the nanoparticle suspension was passed through a syringe filter of 0.45 μm pore size and subsequently washed three times with ultrapure water using a 100 kDa centrifugal filter (EMD Millipore, USA). The PLGA-PEG-PEI nanoparticle concentrate

was diluted with ultrapure water to working concentration and stored at 4° C until use. The nanoparticles were lyophilized with 10% sucrose and stored at -20° C for long-term usage.

Formulation of pcDNA and PEG-PLGA-PEI polyplex. This experiment was designed to evaluate DNA encapsulation at different N/P ratios (number of nitrogen groups in PEI to the phosphate group of the DNA backbone). The plasmid DNA was diluted to 20 µg/mL working concentration, and 25 µl (0.5 µg) aliquots were used for each complexation ratio. Stipulated amounts of PLGA-PEG-PEI nanoparticles (made up to 25 µl with 10% sucrose) corresponding to respective N/P ratios were supplemented with diluted plasmid DNA aliquots and incubated at room temperature for 15 min. A wide range of N/P ratios, starting from 1 to 7, were adopted in the experimental design. At the end of the incubation period, the polyplexes were evaluated by gel retardation assay, and characterized for size and zeta potential (Malvern Zetasizer Nano Z system, Malvern Instruments Ltd., UK) before use in cell culture and animal experiments.

Gel retardation assay. An agarose gel retardation assay was performed to identify the optimum N/P ratio for efficient gene transfer. As per the aforementioned protocol, different N/P ratios (1-7) of polymer/pcDNA complexes were prepared in nuclease free water, and the resultant polyplexes were loaded in 0.7% agarose gel along with the equivalent amount of naked pcDNA as control, and electrophoresed in Mini-Sub® Cell GT Systems at 60 V for 45 min. After the run, the gel was imaged in BioRad Gel Doc™ XR+ Gel Documentation system (Bio Rad, Hercules, CA) to further quantify and analyze the extent of DNA encapsulation.

Uptake of PEG-PLGA-PEI nanoparticles in HCC cells. Cellular uptake of the formulations was evaluated qualitatively and quantitatively using a fluorescence microscope and a flow cytometer analysis of cells treated with coumarin-6 loaded PLGA-PEG NPs, PLGA-PEG-PEI NPs functionalized with Scr peptide, PLGA-PEG-PEI NPs with 10% PLGA-PEG-SP94, PLGA-PEG-PEI NPs with 20% PLGA-PEG-SP94, and PLGA-PEG-PEI NPs with 30% PLGA-PEG-SP94. After 24 h of treatment, the spent media was removed, and the cell monolayer was briefly washed with PBS twice to remove the extracellular unbound nanoparticles. The cells were then stained

with Hoechst 33342 for 5 min and then representative images of each well were acquired using an Olympus IX70 fluorescent microscope under DIC, DAPI, and a green filter. After acquiring representative images of each treatment, the cells were trypsinized and harvested for flow cytometry analysis using a Guava® easyCyte flow cytometer for quantitative estimation of internalized coumarin-6 fluorescence. Around 5,000 events were acquired for each treatment condition and the results were processed using FlowJo analysis software (Tree Star, Ashland, OR, USA) and represented as overlaid histograms of all treatment conditions.

TK-NTR and TK-p53-NTR GDEPT delivered by PEGylated PLGA-PEI nanoparticles in HepG2 and Hep3B cells. The efficiency of PLGA-PEG-PEI nanoparticles-mediated GDEPT of pcDNA-TK-NTR and pcDNA-TK-p53-NTR therapeutic constructs was evaluated in HepG2 and Hep3B cells at 24 h, 48 h and 72 h, in the presence or absence of one or both prodrugs. HepG2 cells and Hep3B cells were seeded at a density of 150,000 cells in each well of a 6-well plate and treated with PLGA-PEG-PEI nanoparticles loaded with 2 μg of pcDNA, pc-TK-NTR, pc-TK-p53-NTR at optimized ratios on the following day. After 24 h, the medium was replaced with fresh medium (DMEM supplemented with 2% FBS, 100 U/mL penicillin and 0.1% streptomycin) and the respective wells were treated with either GCV (1 μg/mL) and/or CB1954 (30 μM). At the end of prodrug treatment time points (i.e. 24 h, 48 h and 72 h), cells were collected by trypsinization and fixed in ice cold 70% ethanol. The fixed cells were washed and stained with PI (15 nM) in the presence of RNase A (10 mg/mL) and 0.01% Triton X100 (Life Technologies, Grand Island, NY, USA); 5,000 events were acquired for each treatment condition and the results were represented as histograms with percentage of live and apoptotic cells.

DNA fragmentation assay. HepG2 cells (60,000 cells/well) were seeded in 12-well plates and incubated at 37 °C overnight, then were treated with pcDNA, pcDNA-TK-NTR and pcDNA-TK-p53-NTR plasmid (2 μg) loaded PEGylated PLGA-PEI nanoparticles. After 24 h of nanoparticle treatment, prodrugs GCV (1 μg/mL) and/or CB1954 (30 μM) were added to the respective wells. The positive control well was treated with 0.5 μM staurosporine for 3 h prior to the completion of 48 h prodrug treatment. At the end of this period all the cells (floating and adherent) were harvested from each well and processed for DNA isolation. The resultant cell pellet was resuspended in lysis

buffer (Tris-HCl (10 mM), NaCl (50 mM), EDTA (5 mM), SDS (0.5% wt/vol), proteinase K (1 mg/mL)) and incubated at 37 °C for 2-3 h. After the incubation period the cell homogenate was supplemented with NaCl to a final concentration of 1M and incubated for 2 more hours followed by centrifugation of the mixture at 14,000 rpm at 4 °C for 15 min. The resultant supernatant was processed for phenol:chloroform:isoamyl alcohol extraction. The aqueous phase was treated with 1/10th volume of sodium acetate (3M, pH 5.4) and 2.5 times volume ice cold alcohol. The mixture was incubated at -80 °C for 30 min and then followed by alcohol precipitation of DNA. The isolated DNA was resuspended in EB buffer and loaded in 1.2% agarose gel and run at 35 V for 3 h for complete resolution of DNA fragments.

Bystander effect of TK-p53-NTR and TK-NTR. To assess the bystander effects of TK-p53-NTR suicide gene therapy, HepG2 cells were treated with TK-p53-NTR loaded PLGA-PEG-PEI nanoparticles and prodrugs as mentioned in the preceding section and at the end of 24 h the treated cells were harvested, washed twice with PBS, and then co-seeded with HepG2 cells stably expressing GFP. Stable GFP expressing HepG2 cells were adapted in this study to distinguish between the two populations of cells in a co-culture during microscopic evaluation, i.e., the cells pre-treated with TK-p53-NTR loaded PLGA-PEG-PEI nanoparticles and the other co-seeded HepG2 cells without any pretreatment. Different ratios of the two cell populations were adopted (20%, 40%, 60%, and 80% treated cells with complementary percentages of untreated HepG2 cells for each case) to draw clear correlations between observed cell viability and bystander effects. Two sets of similar experiments were conducted until this point, after which one batch of treatment was processed for fluorescent microscopy. Here, at the end of 20 h and 40 h, the cells were treated with CytoCy5S (1 ng/mL) substrate followed by Hoechst 33342, and then imaged using fluorescent microscopy under DIC, DAPI, GFP and Cy-5 filters. The other batch of treated cells was processed for flow cytometry analysis of live-dead cells after 24 h and 48 h of PI staining.

Nanoparticle-mediated TK-p53-NTR transfection in 3D-tumor spheroids. To generate 3D-spheroids of cells, we used ultra-low attachment 96-well plates (with dome-shaped bottoms). Briefly, cells were trypsinized after reaching 80-90% confluency and seeded at a density of 5,000 cells per well in 100 µL culture medium. Care was taken to minimize pipette tip contact with the

plate well walls. Spheroids were allowed to form for 5 days under the cell culture conditions. Once this was achieved, fresh culture medium was added, and spheroids were incubated with 2 μg plasmid (TK-p53-NTR) equivalent nanoparticles for 12 h. After nanoparticle administration, individual tumor spheroids were transferred to microfuge tubes for fluorescent staining. Once transferred, tumor spheroids were washed with 0.2 mL of 1X PBS and fixed with 0.2 mL of 4% paraformaldehyde for 10 min, and followed by treatment with 0.2 mL of 4 μg/mL DAPI in PBS for 10 min at room temperature for nuclear staining. Finally, spheroids were washed in 0.2 mL PBS and once in 0.2 mL DI water. Spheroids were then transferred to glass slides and mounted as a suspension in 50 μl PBS. TK-NTR transfected cell distribution through the tumor spheroids was assessed using confocal microscopy (LSM 710, Zeiss), and image analysis was performed using ImageJ software to estimate the depth of penetration. The spheroid images were acquired at different sections under DAPI, GFP and RFP filters to identify the cell nuclei, cell distribution, and NTR converted product of CytoCy5S, i.e. Cy5, respectively.

Immunoblot analysis. To determine the expression of TK in cells treated with TK-NTR, TK-p53-NTR, immunoblot analysis was carried out with anti-TK antibody. Around 50,000 HepG2 cells were seeded in 12-well plates and treated with 1 μg pDNA equivalent at optimized N/P ratio of pDNA (pcDNA, TK-NTR, TK-p53-NTR) and PLGA-PEG-PEI nanoparticles, and after 24 h of treatment, the prodrugs GCV (1 μg/mL) and/or CB1954 (30 μM) were added to the respective wells. After 48 h of prodrug treatment cells were harvested and processed further for immunoblot analysis with anti-TK antibody. In brief, cells were lysed in 100 mL lysis buffer, and 80 μg of total protein from treated HepG2 cells was mixed with β-mercaptoethanol (Bio-Rad) and 10 μl of NuPAGE LDS (4X) loading buffer, heated at 95 °C for 5 min, and loaded in 4-12% SDS-polyacrylamide gel electrophoresis gradient gel (Invitrogen) and run at 80 V for 2 h. The resolved proteins from the gel were then electroblotted onto a 0.2 μm pore size nitrocellulose membrane (Schleicher & Schuell, Keene, NH, USA). The membrane was blocked with 5% non-fat dry milk in tris-buffered saline containing 0.01% Tween-20 (TBS-T, pH 7.6) for 30 min and incubated with the anti-rabbit TK polyclonal antibody overnight at 4 °C on a rocking platform. On the following day, the primary antibody was replaced with peroxidase conjugated goat anti-rabbit IgG secondary antibody (1:10 000 dilution, Rockland Immunochemicals, Gilbersville, PA, USA) after washing it

for 3 × 10 min in TBS-T buffer, and allowed to rock for 2 h. The blots were developed with Pierce ECL Western Blotting Substrate (Thermo Fisher Scientific, USA) and imaged and quantified with the IVIS Lumina III In-Vivo Imaging System.

Hematoxylin and eosin staining. After completion of the gene therapy study time points, all animals were euthanized, and tumors and other organs were excised for H&E *ex vivo* analysis. Excised tissues were fixed in 4% paraformaldehyde overnight at 4 °C and immersed in 70% ethanol, and then embedded in paraffin, sliced at 5 µm thickness in a Leica cryomicrotome (Leica RM2255). Sections were stained in undiluted hematoxylin (Sigma-Aldrich, USA) for 2 min, rinsed in running water, and differentiated in 1% HCl acid/alcohol for 30 s. They were then washed and immersed in bluing solution (Fisher, USA) for 1 min, washed in running water and rinsed in 10 dips of 95% alcohol. After this, slides were counterstained in eosin by dipping into 1:5 ethanol diluted eosin solution (Fisher) for a total of less than 30 s, dehydrated through 95% alcohol, absolute alcohol, and xylene for 5 min each. Slides were mounted with xylene based mounting medium (Permount, Sigma-Aldrich, USA) and imaged using a Nanozoomer (Hamamatsu, Japan).

TUNEL staining for apoptosis measurement. The Hep G2 tumor xenografts of mice treated with TK-NTR and TK-p53-NTR loaded nanoparticles in combination with GCV and CB1954 were assessed for prodrug-induced therapeutic effects by visualizing apoptotic cells in a TUNEL assay. For this, a portion of the tumor was frozen in OCT (TissueTek) and sectioned to 10 µm using a cryomicrotome (Leica CM1850, Wetzlar, Germany). A terminal deoxynucleotidyl transferase (TdT) nick-end labeling (TUNEL) assay was performed with a Trevigen TACS 2 TdT-DAB (diaminobenzidine) *in situ* Apoptosis Detection Kit (TREVIGEN, Gaithersburg, MD, USA) according to the manufacturer's instructions. After staining, the slides were scanned in a Nanozoomer 2.0RS (Hamamatsu, Japan) digital scanner and assessed for diaminobenzidine staining of apoptotic cells using Nanozoomer Digital Pathology software.

Supplementary Results and Discussion

Synthesis and characterization of PLGA-PEG-PEI conjugate polymers, and optimization of PEGylated PLGA-PEI nanoparticles for gene delivery. The L-PEI polymer laden with numerous amine groups was conjugated to the terminal carboxy group of PLGA-PEG polymer using carbodiimide EDC and sulfo-NHS chemistry. EDC couples NHS to carboxyl group, forming an amine reactive NHS ester group that forms an amide bond with the amine groups of PEI **(Fig. 1a-b).** Our initial attempt to use pre-conjugated PLGA-PEG-PEI polymers for nanoparticle synthesis resulted in heterogeneous, unstable nanoparticles with bulky and flexible long chains of PEI that impeded subsequent w/o/w emulsion formation (data not shown). Thus, in the present study we carried out PEI conjugation after the synthesis and stabilization of nanoparticles, which resulted in stable nanoparticles with PEI functionalization limited to the surface of the nanoparticles alone. FTIR analysis of PLGA-PEG-PEI conjugate polymer indicated characteristic peaks of PLGA-PEG at 1767 cm^{-1} (C=O carbonyl stretch), peaks 1089 and 1238 cm^{-1} from the C–O stretch of the ester, along with PEI-associated peaks at 3272 cm^{-1} (–N–H stretching), 2940–2830 cm^{-1} (–C–H stretching), 1576 cm^{-1} (–N–H bending), 1465 cm^{-1} (–C–H bending), and 1350–1000 cm^{-1} (–C–N stretching) **(Fig. 1c)** [3-5]. Apart from these regular peaks arising from PLGA-PEG and PEI, a new peak at 1650 cm^{-1} and 1546 cm^{-1} appeared that corresponded to C=O stretch vibration of the new amide bond formed between the NH_2 group of PEI and COOH group of PLGA-PEG. As a result of this conjugation, the relative intensity of the carboxyl group at 1767 cm^{-1} (C=O carbonyl stretch) and amine group of PEI at 1576 cm^{-1} (–N–H bending) also declined indicating the consumption of these functional groups in new amide bond formation **(Fig. 1c)** [4].

The structure of PEI conjugated PLGA-PEG was further confirmed by 1H NMR analysis **(Fig. 1d)**. The characteristic peaks of PLGA at δ (ppm) = 1.5 ($-CH_3$), δ (ppm) = 4.8 ($-CH_2-$) δ (ppm) = 5.2 ppm (−CH−), and PEG at δ (ppm) = 3.6 ($-CH_2$) were present in the conjugate polymer at the same position as that of precursor indicating no change with the course of the reaction [6]. However, prominent chemical shifts of protons from polyethylene glycol ($–OCH_2\ CH_2–$, 3.65 ppm) and polyethylenimine ($–CH_2\ CH_2\ NH–$, 2.5–2.9 ppm) were observed along with appearance of new peaks at δ (ppm) 2.4 ($-CH_2$ in the proximity COOH group involved in a new amide bond) and 3.2 ($-CH_2$ in the proximity of amine group involved in an amide bond) all clearly indicated that PEI chains were successfully grafted onto -COOH groups of PLGA-PEG [7].

Synthesis and optimization of PEGylated PLGA-PEI nanoparticles. Although PLGA-PEG nanoparticles are well-established nanocarriers for delivery of diverse groups of bioactive molecules, their ability to deliver nucleic acids (RNA and DNA) to cells *in vitro* or *in vivo* is limited by their loading efficiency, stability, and release profile [8]. To counter this setback, we successfully conjugated positively charged PEI moieties on the surface of PLGA-PEG nanoparticles, which drastically improved their DNA loading efficiency (as 4 µg PLGA-PEG-PEI could encapsulate 1 µg DNA, whereas 4.6 µg of PLGA-PEG was required to encapsulate 1 µg DNA), and stability (DNA loaded PLGA-PEG-PEI nanoparticles demonstrated higher zeta potential [+32.4 mV] with lower size PDI [0.274], as compared to PLGA-PEG nanoparticles with -2.3 mV zeta potential and 0.314 size PDI). The presence of PEI facilitates the proton sponge effect for the release of nucleic acids upon internalization into the cells [21]. Furthermore, in order to deliver the therapeutic nucleic acid payload specifically to HCC cells, the nanoparticle surface was impregnated with SP94 targeting peptide moiety **(Fig. 1a)**. The fate of nanoparticles (i.e. bioavailability and biodistribution) in any biological system is largely determined by their size and surface charge. Thus, both size and ζ potential of nanoparticles were estimated at each step of the aforementioned nanoparticle modification process. This also served as an indirect estimate of extent and success of nanoparticle modification **(Fig. 1e, Table S1, S2)**.

The bare PLGA-PEG nanoparticles prepared by the w/o/w solvent evaporation method formed uniform nanoparticles of 147±15 nm diameter, where PEG acts as a hydrophilic corona, while PLGA serves as a hydrophobic core **(Fig. 1e)**. The presence of fractional PLGA on the surface lends the nanoparticle marginal negative charge i.e. –2.3 mV. Subsequently, as a modification to this synthesis process, EDC/NHS activated PLGA-PEG moieties were added to the nanoparticles and then surface functionalized with L-PEI moieties, which led to increases in nanoparticle surface ζ potential to 32.4 mV (indicating the presence of positively charged amine groups of L-PEI on the surface of the nanoparticles). Inclusion of L-PEI moieties on the surface further increased the average particle size to 165 nm with a narrow size distribution (PDI: 0.237). Incubation of plasmid DNA with the positively charged PLGA-PEG-PEI nanoparticles led to formation of stable polyplexes, which corroborated the observed decline in ζ potential to 12 mV.

Different ratios of EDC/NHS activated PLGA-PEG and non-activated PLGA-PEG (i.e. 1:1, 2:3, 3:2) were adapted as precursors for nanoparticle synthesis in order to evaluate their effects on PEI conjugation efficiency, particle size, and ζ potential (table S1). We noted that with higher extent of PEI on the surface of the nanoparticle the ζ potential spiked towards a positive charge, and concurrently, the size of the nanoparticle increased markedly with change in the polydispersity index, indicating that excessive PEI grafting perturbed the nanoparticle stability and size distribution. With this observation, in the subsequent study we used a 1:1 ratio of EDC/NHS activated PLGA-PEG versus non-activated PLGA-PEG. As a final step of modification, targeting peptide (SP94) conjugated PLGA-PEG was also incorporated into the nanoparticles by using a fixed ratio of PLGA-PEG and PLGA-PEG-PEI (maintained at 1:1) with respect to PLGA-PEG-SP94 conjugate polymer as a precursor in the synthesis process. The ratio of other components with respect to SP94 conjugated polymer was optimized for the desired size distribution, DNA encapsulation efficiency, and cellular uptake (table S2). At a higher proportion of SP94 conjugated polymer, e.g. at 1:2, the nanoparticle ζ potential declined by 6 mV indicating that a relatively lower amount of L-PEI could be incorporated on the nanoparticle surface. This observation was also validated from the findings of the DNA gel retardation assay of respective nanoparticles **(Fig. 1f, Fig. S1)**. Another observation from the two experiments outlined in table S1 and table S2 was that the extent of L-PEI incorporation in the nanoparticle (indicated by the ζ potential) was dependent on the fraction of EDC/NHS activated PLGA-PEG in the precursor, which indirectly confirmed that L-PEI was incorporated only by means of chemical conjugation and not by electrostatic adsorption.

In our earlier studies, we reported the synthesis of PLGA-PEG/PEI nanoparticles for gene therapy, wherein mere electrostatic adsorption of PEI on the PLGA-PEG nanoparticles was adopted. In such a strategy, there was a possibility of hampering the nanoparticle stability upon addition of negatively charged nucleic acids, since the partial negative charge of PLGA-PEG nanoparticles would compete with the much higher negatively charged nucleic acid for the amine groups of PEIs. That would weaken the electrostatic adsorption of L-PEI layer on the surface of the nanoparticles [8]. In order to avert these competitive electrostatic interactions, herein we used covalently conjugated PEI as well as electrostatic interaction for plasmid encapsulation.

The FE-SEM observation of SP94 and PEI incorporated PLGA-PEG nanoparticle clearly depicts uniform nanoparticles with narrow size distribution, which is well in line with the DLS measurements **(Fig. 1g)**. The FE-SEM images of nanoparticles and PEI complexes show rough surfaces studded with abrupt protrusions of DNA polyplexes **(Fig. 1h).**

Gel retardation assay measures the DNA to nanoparticles ratio necessary for efficient transfection. The electrostatic interaction between positively charged PEI moieties on the nanoparticles and negatively charged nucleic acid leads to effective condensation of DNA into polyplexes on their surface. The net charge of these polyplexes and plasmid encapsulation efficiency are determined by the ratio of the nanoparticle and DNA (i.e. N/P ratio). Thus, polyplexes of different N/P ratios (0.4 to 4 μg weight NPs) were evaluated by gel retardation assay to optimize the DNA encapsulation efficiency with 1.0 μg of DNA **(Fig. 1f)**. We observed that with increase in nanoparticle proportion in the polyplex, the electrophoretic mobility of DNA was retarded in the case of polyplexes with 0.4 μg and 0.78 μg nanoparticles (conjugate polymer weight equivalent), gradually indicating progressive condensation and neutralization of plasmid on the surface of the nanoparticles. For polyplexes with 4 μg nanoparticles, the plasmid was completely condensed and retained in the well, and this trend continued at higher concentrations. Although the plasmid was completely encapsulated in the polyplexes, its transfection efficiency would determine the optimum N/P ratio for efficient gene delivery.

Transfection efficiency of PLGA-PEG-PEI nanoparticles in HCC cells. We used flow cytometry and optical bioluminescence imaging for evaluating the level of transfected gene expression, whereas we determined the absolute copy numbers of plasmid DNA delivered to HCC cells using real time PCR. Flow cytometry and optical bioluminescence imaging of HepG2 and Hep3B cells treated with FLuc-EGFP (2 μg) plasmid and PLGA-PEG-PEI nanoparticle polyplexes of different N/P ratios led to distinct patterns of variation in EGFP and FLuc expression levels **(Fig. S3 and S4)**. At the outset, the trend of transfection efficiency estimated by quantification of EGFP expressing HepG2 cells matched well with the trend observed in results of the FLuc assay. We observed that the transfection efficiency increased initially, i.e. from 34.7% to 68% for 2:1 to 4:1 NP/DNA ratio and then declined to 22.4% at a higher N/P ratio (i.e. at 8:1 ratio). The cells

treated with 4:1 weight ratio of NP/DNA showed highest transfection efficiency of 67% (EGFP expression) which also achieved 2.6-fold higher bioluminescence (p<0.001) in the FLuc assay as compared to that of commercial Lipofectamine 2000 transfection reagent used at the ratio suggested by the manufacturer **(Fig. S3 and S4)**.

***In vitro* targeted delivery of pDNA using SP94 conjugated PLGA-PEG-PEI nanoparticles in HCC cells.** We evaluated the effect of SP94 targeting ligand on the specificity of HCC cell transfection using Coumarin-6-loaded PEGylated PLGA nanoparticles, and the results were compared to non-targeted particles at 24 h post transfection **(Fig. S5)**. The scrambled peptide (ScSP94)-functionalized PLGA-PEG-PEI nanoparticles loaded with Coumarin-6 were used as control. Post-treatment analysis of cells showed that approximately 24% of HepG2 cells were fluorescently labeled when incubated with ScSP94 peptide conjugated PLGA-PEG-PEI nanoparticles at the end of 24 h; whereas in the case of SP94 conjugated PLGA-PEG-PEI nanoparticles, relatively higher extents of cellular uptake were observed (i.e. ~47%, ~42%, ~33% in the case of 10% PLGA-PEG-SP94 (p<0.001), 20% PLGA-PEG-SP94 (p<0.001) and 30% PLGA-PEG-SP94 (p<0.01) conjugated variants of PLGA-PEG nanoparticles, respectively). Interestingly, the nanoparticles with 10% of SP94 conjugated PLGA-PEG nanoparticles showed the maximum uptake, i.e. 47%, which was higher than nanoparticles with 30% SP94 conjugated PLGA-PEG conjugate polymer, i.e. 33%. A possible explanation for this is that presence of excessive peptide moieties on the nanoparticle surface leads to steric hindrance for ligand-receptor binding/interaction, which could limit the receptor-mediated uptake of nanoparticles [9]. Furthermore, the size and zeta potential analysis of nanoparticles with 30% of PLGA-PEG-PEI-SP94 were larger in size and with a higher polydispersity index, indicating that inclusion of a higher fraction of SP94 counterpart in the nanoparticle destabilized it and could contribute to the observed trend **(Table S2)**. It is challenging to fully understand the mechanisms behind the difference in internalization kinetics of these particles given that the receptor responsible for binding and internalization of SP94 peptide by HCC cells has not been identified to date [10].

Estimation of PLGA-PEG-PEI NPs threshold DNA payload capacity for TK-NTR and TK-p53-NTR by YOYO-1 dye mediated FACS analysis. DNA loading efficiency experiment was further used to reveal the DNA binding efficiency of TK-53-NTR plasmid. We used increasing

amount of pDNA inclusion in complexation with stipulated quantity of NPs (4 μg), the extent of YOYO-1 fluorescence associated with the nanoparticles initially increased periodically, indicating progressive increase in fraction of pDNA loaded in the nanoparticles (**Fig. S2**). The YOYO-1 stained pDNA content in NPs increased significantly ($P \leq 0.05$) up to 0.75 μg of pDNA and then began to saturate with higher pDNA content. Furthermore, at the highest fraction of pDNA i.e. 1.75 μg the histogram began to shift towards the higher fluorescence indicating the threshold pDNA loading level in NPs. Gel electrophoresis of these pDNA-NPs complexes corroborated this observation, indicating that, initially, with increase in fraction of pDNA, higher fractions of pDNA were loaded in the nanoparticles that began to saturate after 1 μg pDNA for 4 μg of NPs, leading to release of excess unencapsulated pDNA present in complexes at higher DNA fractions.

Estimation of TK-NTR and TK-p53-NTR pDNA delivery using PLGA-PEG-PEI nanoparticles in HCC cells measured using CytoCy5S imaging. To establish the functional efficacy of TK-NTR and TK-p53-NTR genes delivered using PLGA-PEG-PEI nanoparticles, we used 2 μg of DNA at optimal N/P ratio (4:1) that was further confirmed for complexation, delivery, and cell toxicity **(Fig. S6)**. We used CytoCy5S imaging to evaluate the functional effect of NTR using fluorescence microscopy and FACS analysis, and immunoblot analysis of the expression of the fusion protein. At the end of 48 h treatment, the HepG2 and Hep3B cells were supplemented with NTR substrate CytoCy5S (1 ng/mL) and incubated for 3 h and then observed for Cy5 signal under a fluorescent microscope **(Fig. S7)**. CytoCy5S is the substrate of NTR enzyme, which catalyzes the conversion of quenched CytoCy5S into a reduced form that is a red-shifted fluorescent dye stably retained within the cells as a non-toxic imaging agent [10]. The expression of fusion proteins TK-NTR and TK-p53-NTR in HepG2 and Hep3B cells was confirmed by measuring fluorescent signals of CytoCy5S (reduced form) under Cy5 filters, which quantitatively established the extent of gene delivery, whereas in the case of control cells treated with pcDNA loaded nanoparticles, no fluorescence signal was observed. Subsequent FACS analysis of these cells for CytoCy5S fluorescence revealed cell population distributions over a broad fluorescent range, with nearly 53% of the cells treated with TK-NTR and 64% of cells treated with TK-p53-NTR exhibiting higher fluorescence than the control cells **(Fig. S7)**. Cell population histograms clearly indicated two distinct populations corresponding to those with and without CytoCy5S, representing the extents of transfection and functional enzyme expression levels.

On the other hand, the expression of TK as well as exogenous p53 was confirmed by immunoblot analysis of total cell proteins with anti-p53 and anti-TK antibodies **(Fig. S9)**. Anti-TK antibody generated distinct bands at 42 kDa and 57 kDa corresponding to TK (42 kDa) and TK-NTR fusion protein (57 kDa). Similarly, probing with anti-p53 antibody revealed three distinct bands corresponding to TK-p53-NTR (104 kDa), p53-NTR (68kDa), as well as the band for p53 (53 kDa). Thus, the expression profiles of the proteins encoded by the triple gene validate successful delivery of the TK-p53-NTR gene using PLGA-PEG-PEI nanoparticles.

Quantitative estimation of intracellular plasmid copy numbers by real-time PCR in HCC cells transfected with TK-NTR and TK-p53-NTR using PLGA-PEG-PEI nanoparticles. The therapeutic efficacy of GDEPT crucially relies on the efficiency of gene delivery [11]. Thus, dose dependent uptake for both TK-NTR and TK-p53-NTR plasmid was evaluated at the pre-optimized N/P ratio for different payloads of plasmids (TK-NTR or TK-p53-NTR), i.e. 0.5 µg, 1 µg, 1.5 µg, 2 µg, 2.5 µg and 3 µg for a given number of cells **(Fig. S6)**. We found that for both TK-NTR and TK-p53-NTR plasmids, similar trends in extents of plasmid internalization were achieved with respect to plasmid dosage levels. At the minimal dosage of 0.5 µg plasmid loaded nanoparticles, the internalized copy number was estimated to be 4.7×10^{10} and 4.54×10^{10} for TK-NTR and TK-p53-NTR, respectively. A prominent increase in intracellular plasmid copy number was observed for the 1 µg plasmid dosage that subsequently peaked to a value of 1.76×10^{11} and 1.29×10^{11} copy numbers for TK-NTR and TK-p53-NTR plasmids ($p<0.001$), respectively, at 1.5 µg plasmid dose. At higher dose of plasmid, i.e. above 2 µg, the copy number gradually declined to a value close to 8×10^{9} copies ($p<0.01$).

Assessments of cell viability at the conclusion of treatment also provided a clear explanation for the observed trends in plasmid delivery. These demonstrated that polyplexes at the same N/P ratio inflict cellular concentration-dependent cytotoxic effects that become prominent at doses higher than 1.5 µg plasmid dose (for 150,000 cell-seeding density), and thereby identifies the extent of plasmid to PLGA-PEG-PEI ratio needed for successful delivery of DNA without toxicity **(Fig. S6)**. The majority of dead cells observed at higher concentrations of polyplex arise as a result of polyplex uptake, and thus a significant portion of the polyplexes are excluded from the cell

internalization analysis, since dead cells are eliminated during cell harvest. Thus, at lower polyplex concentrations (i.e. 0.5 µg, 1 µg, and 1.5 µg) the internalized plasmid copy number is dose dependent and it declines at higher concentrations where cytotoxicity of polyplexes becomes the governing factor. Thus, an upper limit for polyplex dosage should also be considered to avoid any nonspecific cytotoxic effects.

Cell cycle analysis demonstrates the therapeutic effect of TK-p53-NTR gene therapy delivered using PLGA-PEG-PEI nanoparticles in response to GCV-CB1954 prodrug combination in HCC cells. Flow cytometry cell cycle analysis was performed to study the effects of gene therapy by estimating different phases of cell cycle status after different treatment conditions **(Fig. 2d)**. In control cells treated with the prodrugs GCV and CB1954, and pcDNA-loaded PLGA-PEG-PEI nanoparticles, 69.3% of the cells were in G0/G1 phase, 8.6% cells were in S phase, and 20.6% cells in G2 phase. In cells treated with TK-NTR/TK-p53-NTR plasmid-loaded nanoparticles plus prodrugs, the distribution of cell populations was prominently disrupted as a result of interference of CB1954 and GCV metabolites with the host DNA synthesis. The 2- and 4-hydroxylamines metabolites resulting from NTR-mediated conversion of 5-Aziridino-2,4-dinitrobenzamide (CB1954) formed stable crosslinks with host DNA and led to irreparable DNA damage that subsequently instigated apoptosis. Thus, CB1954/NTR GDEPT manifests its cytotoxic effects irrespective of the phase of the cell cycle (i.e. in both dividing and non-dividing cells), which led to accumulation of nearly 20.3% cells in the S phase, as compared to 8.6% in the control cells [12]. In the case of TK/GCV GDEPT the active drug GCV triphosphate (a nucleoside analogue) is effective only against dividing cells actively synthesizing DNA (i.e. cells in the S phase), as a result of which, cells in the G2 phase gradually become the predominant surviving population—these increased to 60.3%, as compared to control cells with only 20.6% of cells in G2. These dormant cells in the G2 phase are often responsible for GCV resistance even after prolonged treatments. In this study we circumvented this limitation by a strategic combination with the NTR/CB1954 system to target both dividing and non-dividing cells simultaneously [13]. As an outcome of this combination gene therapy, co-treatment with both prodrugs led to suppression of both G0/G1 and G2 populations, as well as S phase arrest of cancer cells.

DNA fragmentation assay reveals a strong apoptosis mediated DNA damage in cells transfected with TK-NTR or TK-p53-NTR and exposed to GCV-CB1954 prodrug therapy. DNA fragmentation is a biochemical hallmark of apoptotic cell death. Agarose gel electrophoresis of DNA isolated from untreated or bare nanoparticle-treated HepG2 cells in the presence of prodrugs produced sharp bands corresponding to intact genomic DNA (gDNA), whereas in case of cells treated with TK-NTR or TK-p53-NTR loaded nanoparticles functionalized with or without SP94, extensive DNA laddering and smearing effect was observed, depicting the damage to chromatin. Further scrutiny for an 'oligosomal ladder' pattern was positive for ~180 bp inter-nucleosomal excision, which is a characteristic feature of later stages of apoptosis. A highly effective apoptotic inducer, staurosporine (protein kinase inhibitor) manifested similar DNA laddering effect. The relatively higher molecular weight mass DNA fragments (> 50 kb in length) in the smear were an outcome of higher order chromatic cleavage induced in the early apoptotic stages by the mitochondrial nuclease EndoG. On the other hand, the regularly spaced ladder DNA was an outcome of single stranded spaced nicks at nucleosomal and subnucleosomal periodicities mediated by the concerted effect of initiator caspases (caspase-2, -8, -9 and -10) and executioner caspases (caspase-3, -6 and -7). The upregulation of initiator and executioner caspases is an outcome of release of cytochrome C from mitochondria in the event of p53-mediated upregulation of bad, bax and bak proteins **(Scheme 1, Fig. 4)**. The extent of DNA fragmentation was significantly higher in the case of TK-p53-NTR as compared to TK-NTR, clearly suggesting that p53 augments apoptosis by caspase activation through bad, bax and bak mediated mitochondrial cytochrome C release, which also supports the findings of the immunoblot analysis.

TK-NTR gene therapy delivered using PLGA-PEG-PEI nanoparticles showed significant bystander effects when treated with GCV-CB1954 prodrug combination in HCC cells as measured by fluorescent microscopy of CytoCy5S. In addition to FACS analysis results of bystander effects shown in **Fig. 2e**, we also measured a visual validation of the bystander effect in cell culture using fluorescent microscopic analysis. To distinguish the two populations of HepG2 cells in the co-culture study, control HepG2 cells with stable EGFP expression was used, whereas the GCV and CB1954 (24 h) prodrug treated population of HepG2 cells pre-transfected with TK-p53-NTR were pre-incubated with fluorescent substrate CytoCy5S for 4 h to track the TK-p53-NTR expressing cells. The prodrug analogue CytoCy5 not only enables the tracking of TK-p53-

NTR expression in cells under a Cy5 filter but also enables tracking its diffusion into control cells in their proximity identified as stable GFP expressing cells. Thus, GFP expressing cells with red fluorescent CytoCy5 also retained within them were an outcome of intercellular diffusion of activated prodrug—a dynamic prerequisite in the bystander effect. The representative images of different co-culture compositions acquired by fluorescence microscopy under GFP, DAPI and Cy5 filters categorizes the cells into four different populations, i.e. GFP expressing control cells, treated cells expressing TK-p53-NTR, and treated cells without TK-p53-NTR expression (identified by Hoechst 33342 alone stained nucleus) **(Fig. S12)**. At 24 h and 48 h a characteristic fourth cell population identified with fluorescence under both GFP and Cy5 filters (which appeared as yellow color population in the overlay of images acquired under green and red filters) became more prevalent, indicating higher instance of activated drug diffusion from nearby dead cells. This mirrored the findings of higher percentages of cell death owing to the bystander effect seen with flow cytometry.

Immunoblot analysis of signaling proteins and validation of apoptosis induction demonstrated by DNA fragmentation assay showed TK-p53-NTR mediated therapeutic improvement in HCC cells. The downstream therapeutic manifestations of the delivered TK-p53-NTR gene is preceded by expression of TK, NTR and p53 proteins in the tumor cells. We therefore studied these expressions using immunoblot analysis **(Fig. 4a,b)**. Although p53 protein expression in both TK-NTR and TK-p53-NTR treated cells was higher than control cells, it was much higher (by nearly 5-fold) in TK-p53-NTR treated cells as a consequence of exogenous p53 supplementation. The increase in p53 protein level is not solely the outcome of introducing exogenous p53 but also partially owing to the stabilization of endogenous p53 protein through change in signaling cascade in cells treated with suicide genes plus prodrug combination. Hence, p53 upregulation was also observed in the case of cells delivered with TK-NTR. In the case of TK-p53-NTR treatment alone, apart from p53 specific protein bands at 53 kDa, two additional distinct bands at higher molecular weight appeared upon probing with the p53 antibody, which corresponded to partial cleavage of fused proteins TK-p53 and TK-p53-NTR from the fusion protein expressed with P2A slippage sequence. This was further confirmed by anti-TK antibody which also detected bands exactly at these two specific positions **(Fig. 4a,b)**.

p53 protein plays a pivotal role in apoptosis by regulating downstream apoptotic signaling proteins such as bax, bad and bak [14]. Bax protein expression was observed to increase by nearly 4-fold in case of TK-p53-NTR (p<0.001), and 2.8-fold (p<0.001) in case of TK-NTR **(Fig. 4b)**. Bax and bak proteins act in concert to architect oligomeric pores in outer membranes of mitochondria (mitochondrial outer membrane permeabilization, MOMP) which leads to loss of its membrane integrity and subsequent release of cytochrome C[15]. Cytochrome C then activates the caspase family of genes leading to an irreversible commitment towards cell death. A major effector or executioner of this class of proteins is caspase-3 which orchestrates nuclear fragmentation, a signature event of apoptosis [16]. We therefore observed that the expression levels of caspase-3 and bax were distinctly higher (p<0.001) for both TK-NTR and TK-p53-NTR treatments, but with much higher levels in cells transfected with TK-p53-NTR (p<0.05), clearly suggesting that activation of apoptotic pathways are a major contribution to the observed cell death in the triple gene therapy. Apart from this, for both TK-NTR and TK-p53-NTR, treatment using CB1954 and GCV demonstrates consistently higher expression levels of pro-apoptotic proteins bax, p53 and caspase-3 (p<0.001), which mirrors the synergistic antiproliferative effects of triple gene therapy observed in the apoptotic analysis **(Fig. 4a,b)**. While pro-apoptotic protein expression increased, a marginal decline in anti-apoptotic Bcl-2 and increase in cytostatic p21 were also observed [17]. In contrast, no significant change in p65, a protein involved NF-κB mediated survival signaling, was observed[18]. The results of the DNA fragmentation assay revealed a strong apoptosis-mediated DNA damage in cells treated with either TK-NTR or TK-p53-NTR in combination with GCV/CB1954 mediated gene therapy compared to control cells **(Fig. 4c).**

***Ex vivo* CytoCy5S imaging, TUNEL staining and histological analysis revealed the successful gene delivery and therapeutic effect *in vivo*.** To confirm the gene-prodrug delivery associated therapeutic effect in HCC *in vivo*, we performed ex vivo analysis of tumor tissues for CytoCy5S fluorescence signal, TUNEL staining for induced apoptosis cells, and histology for treatment associated toxicity in different organs. In both control and treated groups, tumors were excised and inspected by histological staining with hematoxylin and eosin (**Fig. 6f**). In the control group, the tumor cells were closely aligned and possessed bigger cell nuclei and higher nuclear/cytoplasm ratios than those in the other four groups. However, in the case of mice treated with TK-NTR or

TK-p53-NTR plus prodrugs CB1954 and GCV, cancer cells exhibited sparse arrangement, cell shrinkage, fragmentation, and chromatin disappearance, indicating dispersed necrosis, apoptosis and inflammation, which were much more prevalent in the case of TK-p53-NTR than TK-NTR. As elucidated in *ex vivo* tissue imaging, the delivery and expression of gene therapy vectors corresponded to the topological distribution of fluorescent product generated by NTR-catalyzed conversion of CytoCy5S. Thus, expression levels of TK-NTR in different tumors was assessed in different treatment groups under Cy5 filter of a fluorescence microscope. We observed that the CytoCy5 stained tumor sections predominantly coincided with apoptotic populations of cells, indicating that the expression levels of gene vectors corresponded closely to the dead or dying populations of cells in tumor tissues. Terminal deoxynucleotidyl transferase-mediated dUTP nick end-labeling (TUNEL) assay of tumor sections revealed the extent of apoptosis in control and treated groups (**Fig. 6f**). The localized distribution pattern of CytoCy5S fluorescent substrate coincided with regions of higher apoptosis as observed in TUNEL assay which clearly asserts the anticancer therapeutic potential of TK-NTR/TK-p53-NTR gene therapy against HCC. Furthermore, as observed in *in vitro* DNA fragmentation assay, significantly higher extents of apoptotic cell populations were observed in the case of TK-p53-NTR treated tumor as compared to that of untreated control cells, which establishes the role of p53 in augmentation of TK-NTR suicide gene mediated apoptosis in *in vivo* HCC xenograft mouse models.

Supplementary Figures

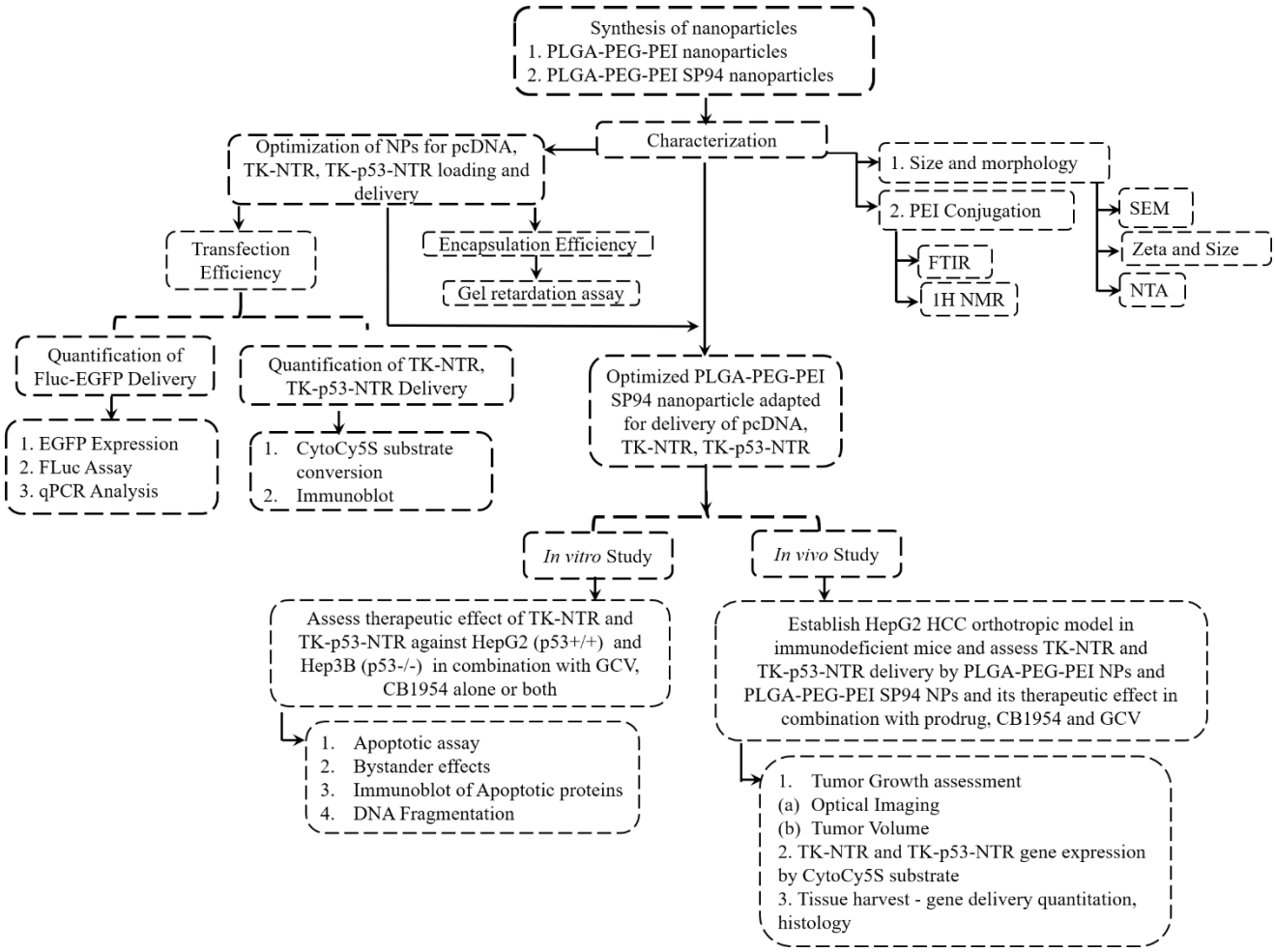

Scheme S1: Schematic outline of the study workflow.

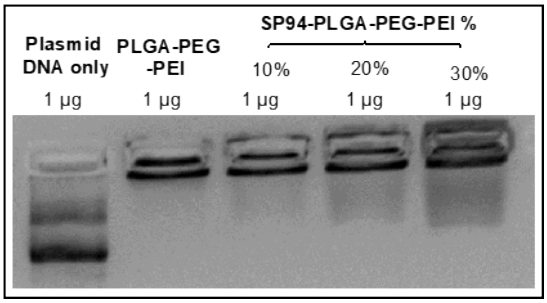

Fig. S1: PLGA-PEG-PEI NPs DNA encapsulation efficiency; DNA encapsulation efficiency of PLGA-PEG-PEI nanoparticles (NP: 4 µg + DNA 1 µg), with and without SP94 targeting peptide.

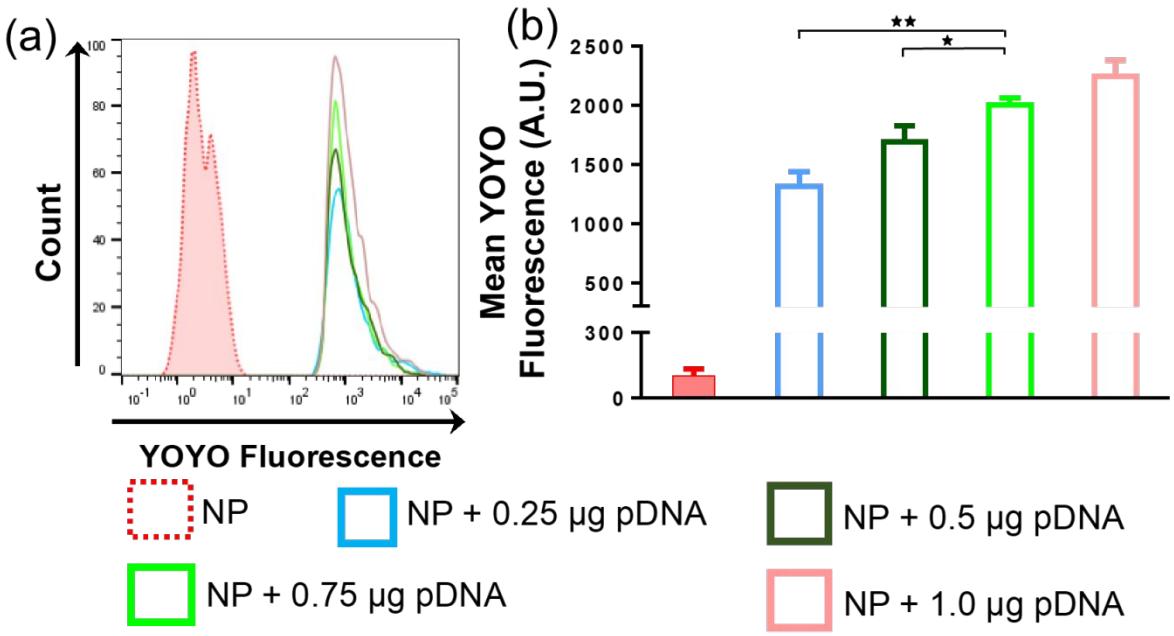

Fig. S2: DNA loading efficiency by PLGA-PEG-PEI nanoparticle measured by YOYO-1 DNA binding dye by FACS **(a)** and respective mean fluorescence signal plot **(b)**.

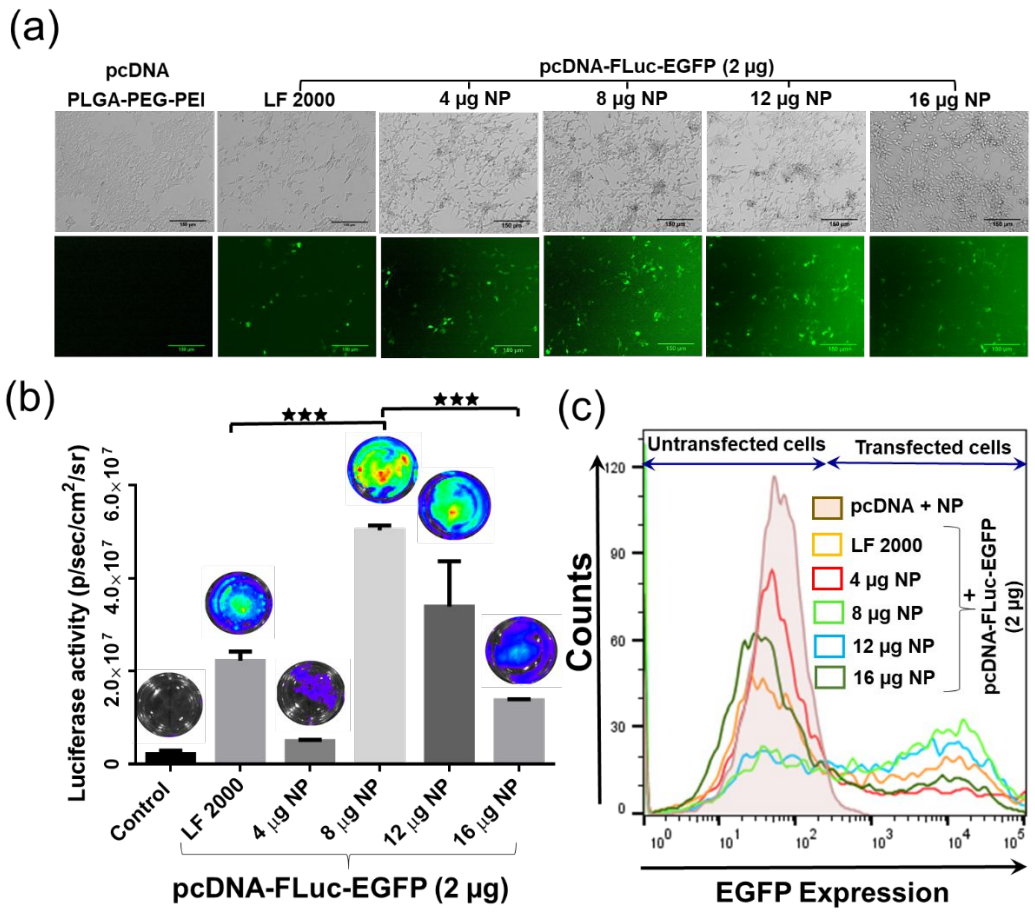

Fig. S3: ***In vitro*** **evaluation FLuc-EGFP Plasmid DNA delivery by PLGA-PEG-PEI nanoparticles in HCC cells. (a)** Microscopic images (Brightfield and GFP filter) of HepG2 cells transfected with FLuc-EGFP plasmid loaded in PLGA-PEG-PEI NPs at different N/P ratios and corresponding Luciferase assay images with quantitative graph **(b)** and EGFP flow cytometry analysis results **(c)**.

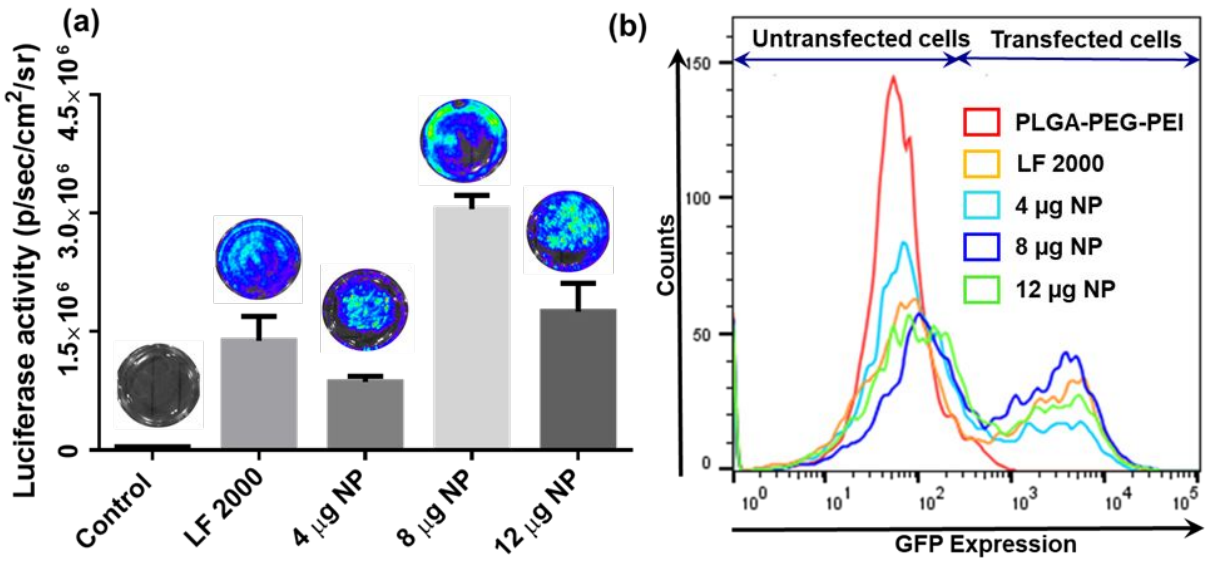

Fig. S4: PLGA-PEG-PEI NPs transfection efficiency in Hep3B; (a) FLuc assay of Hep3B cells transfected with Fluc-EGFP plasmid using PLGA-PEG-PEI nanoparticles with different N/P ratios of polyplexes and corresponding **(b)** flow cytometry analysis. The data are presented as mean ± SEM; * represents $p<0.05$, ** represents $p<0.01$ and *** represents $p<0.001$.

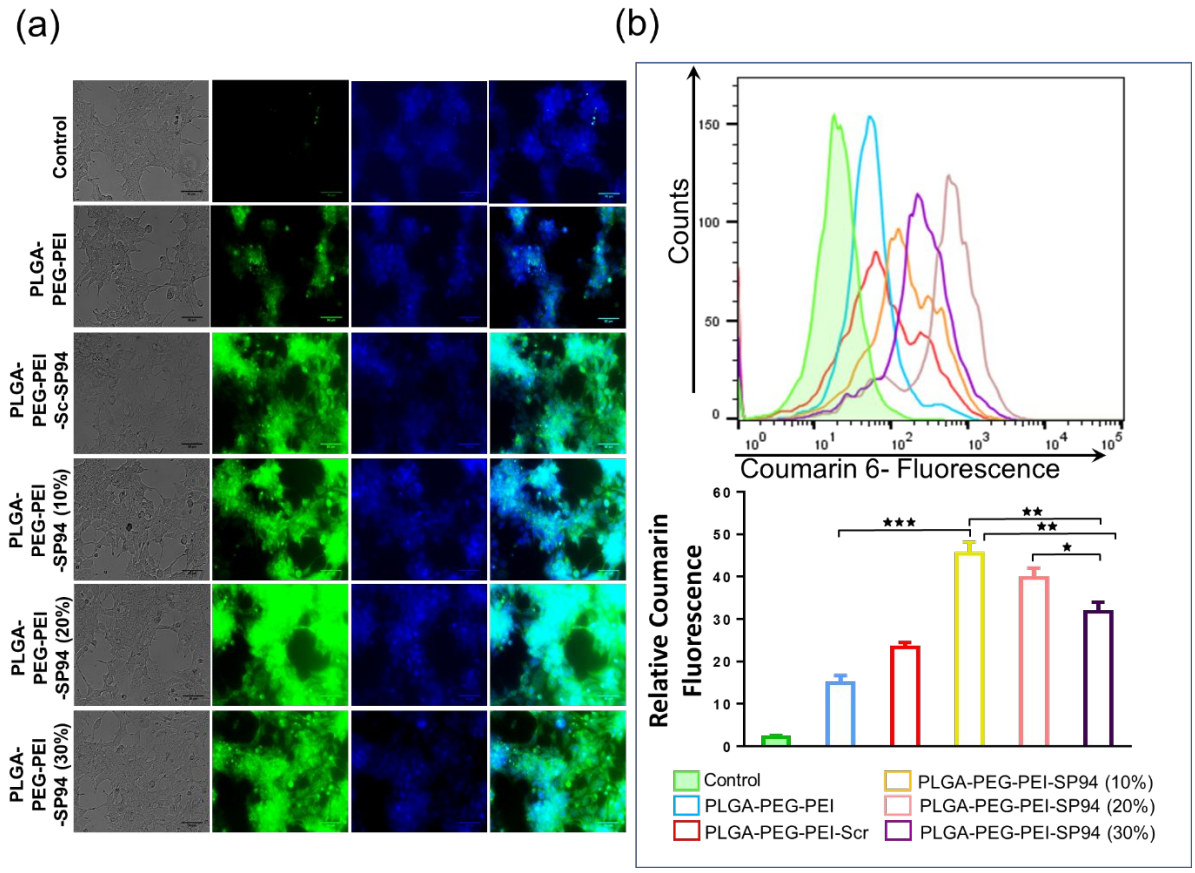

Fig. S5: Estimation of Coumarin-6 loaded PLGA-PEG-PEI nanoparticles and SP94 functionalized PLGA-PEG-PEI nanoparticles (10%, 20%, 30%) uptake in HepG2 cells by microscopic **(a)** and flowcytometry analysis **(b)**.

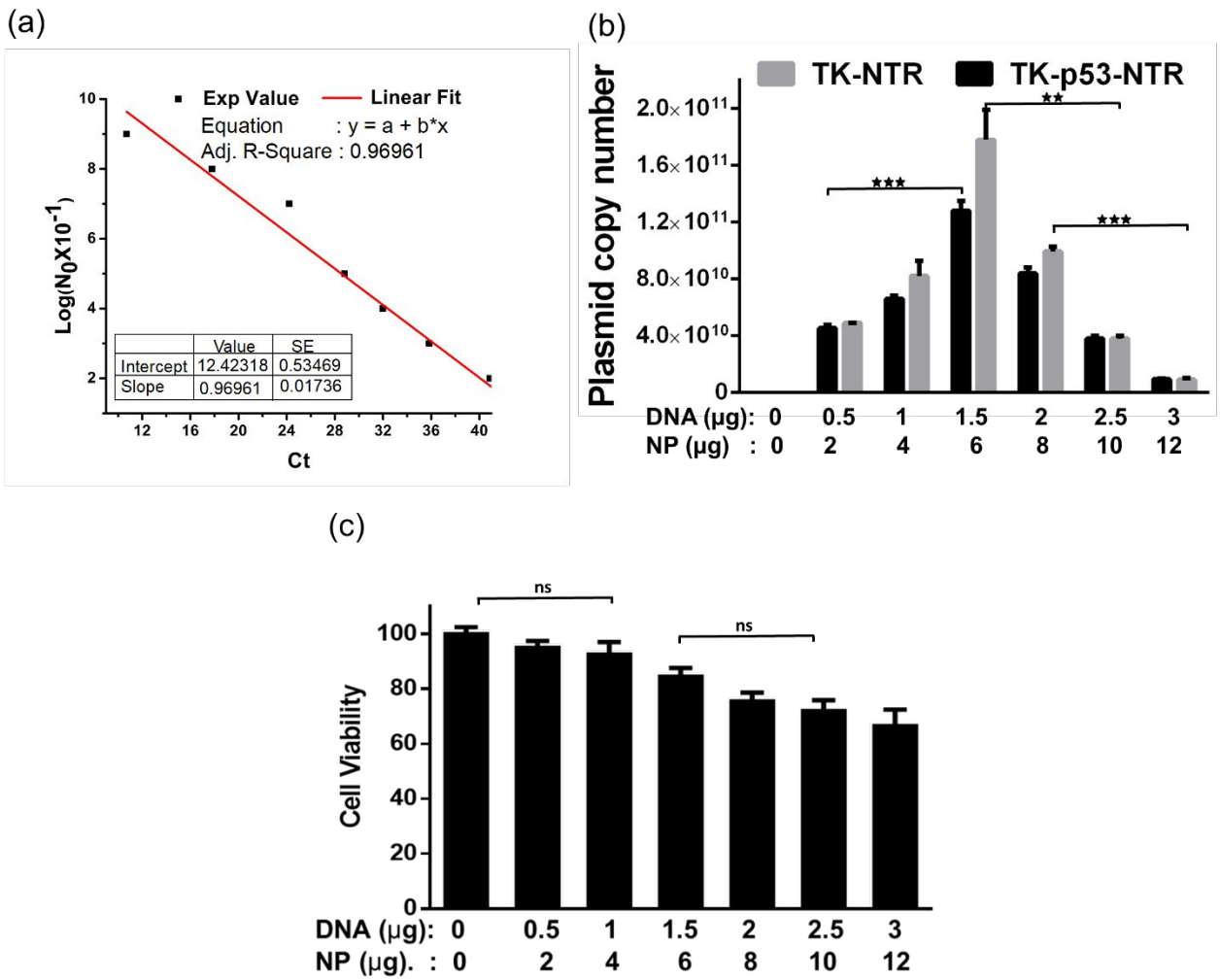

Fig. S6: (a) Standard graph for estimation of TK-p53-NTR plasmid copy number with Ct value in qPCR analysis. **(b)** Quantitative estimation of dose dependent TK-NTR/TK-p53-NTR plasmid transfection in HepG2 cells by PLGA-PEG-PEI nanoparticles. **(c)** Cell viability in HepG2 cells after transfection with different N/P ratios of plasmid to NP combinations shown in **'b'**.

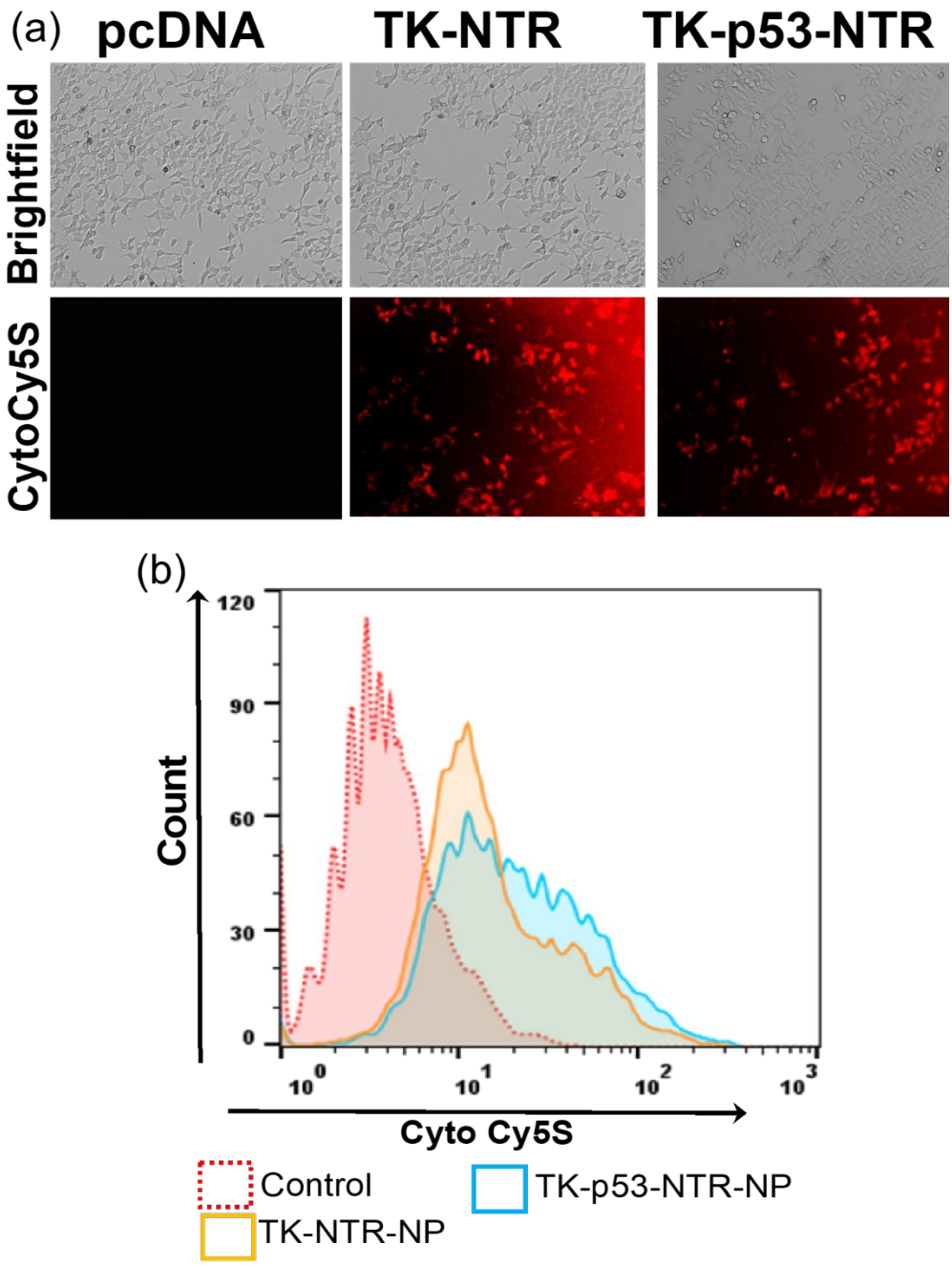

Fig. S7: CytoCy5S substrate conversion in HepG2 cells transfected with TK-NTR and TK-p53-NTR plasmid by PLGA-PEG-PEI nanoparticles assessed by fluorescence microscopy **(a)**, and flow cytometry **(b)**.

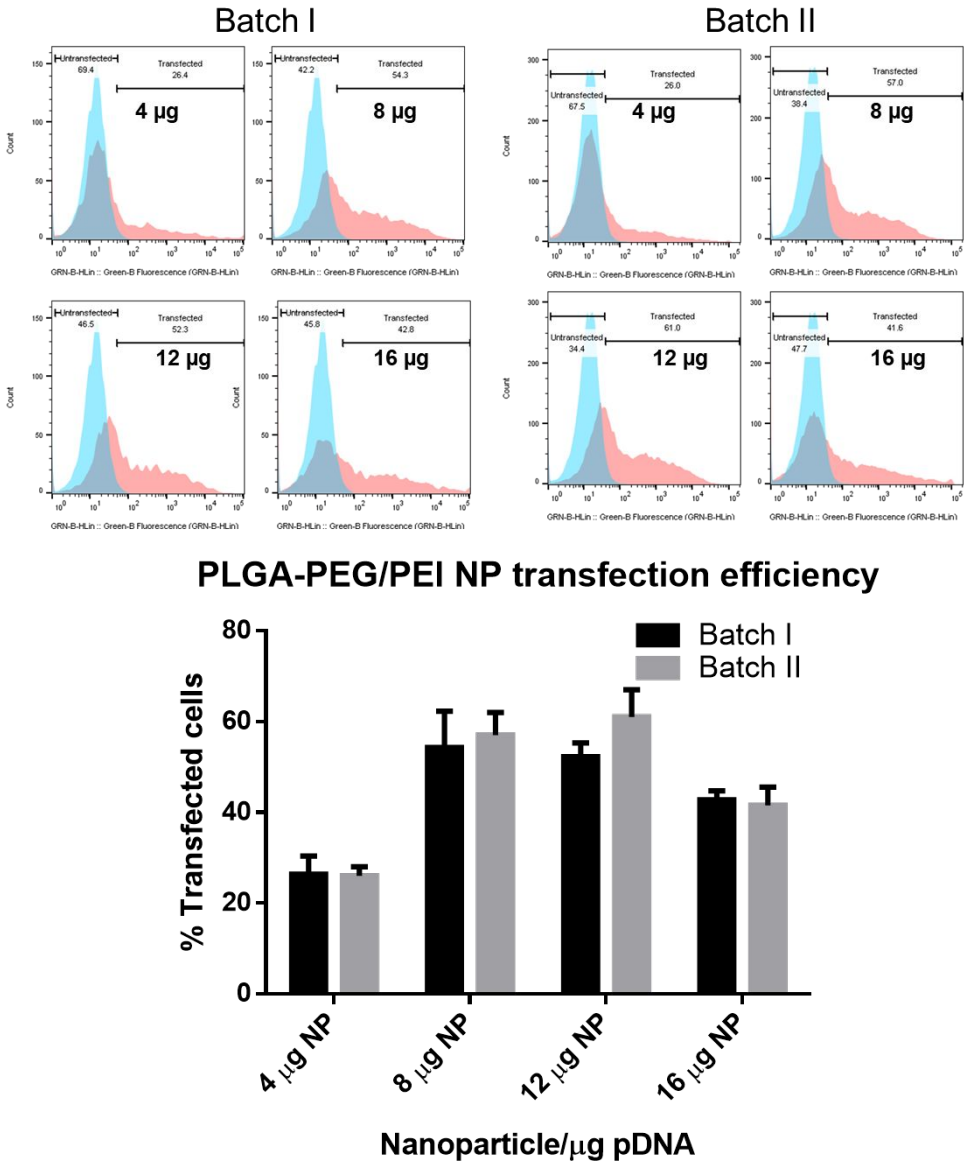

Fig. S8: Transfection efficiency variation between different batches of PLGA-PEG-PEI NPs. Comparative estimation of transfection efficiency of PLGA-PEG-PEI nanoparticles of different synthesis batches for evaluation of consistency in efficacy of nanoparticle-mediated gene delivery. The data are presented as mean ± SEM; * represents $p<0.05$, ** represents $p<0.01$, *** represents $p<0.001$ and ns represents not significant.

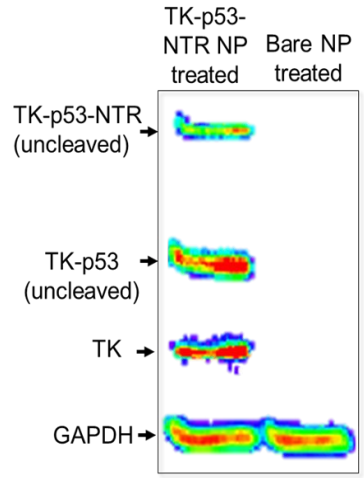

Fig. S9: Immunoblot assay of the TK-p53-NTR proteins expressed in HepG2 cells transfected with the TK-p53-NTR plasmid DNA loaded in PLGA-PEG-PEI NPs.

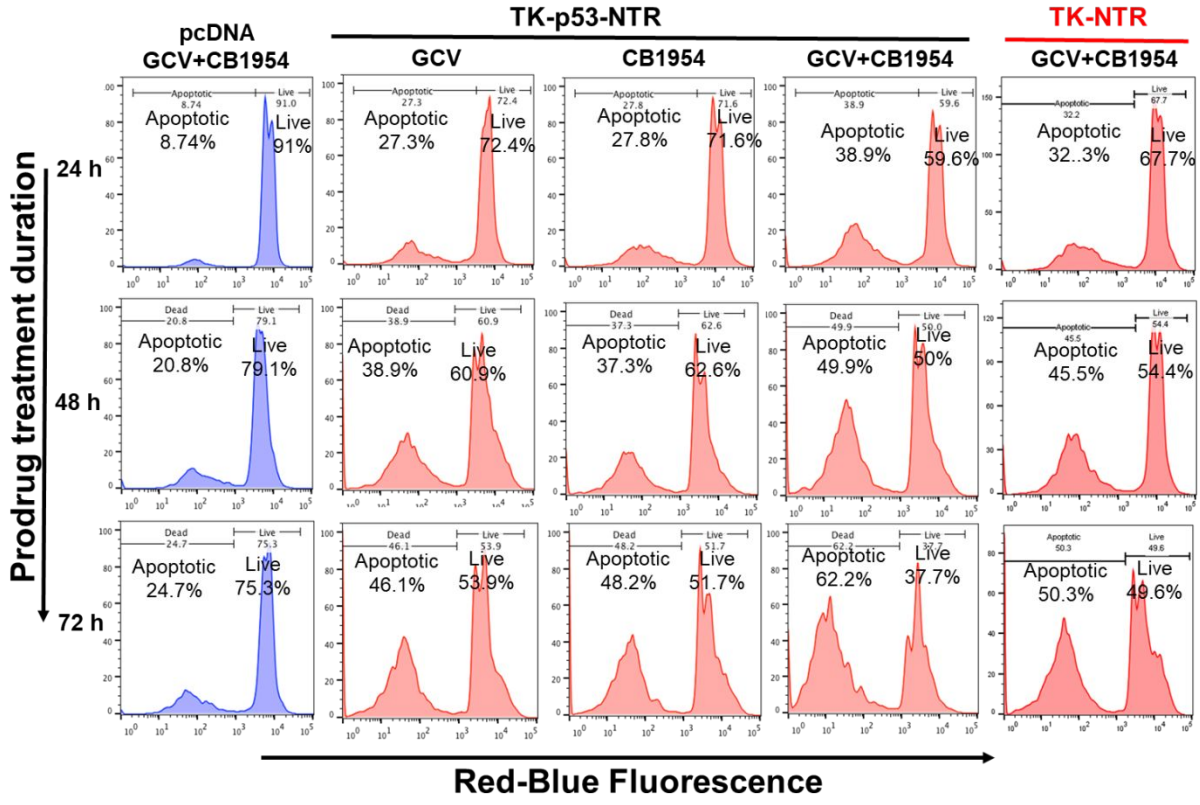

Fig. S10: TK-p53-NTR therapeutic efficacy in HepG2 Cells. PI staining-based flow cytometry assay measures apoptotic population at different time points (24 h, 48 h and 72 h) after HepG2

cells after delivered with pcDNA, or pcDNA-TK-NTR, or pcDNA-TK-p53-NTR by PLGA-PEG-PEI nanoparticles and treated with GCV and/or CB1954 prodrugs combination.

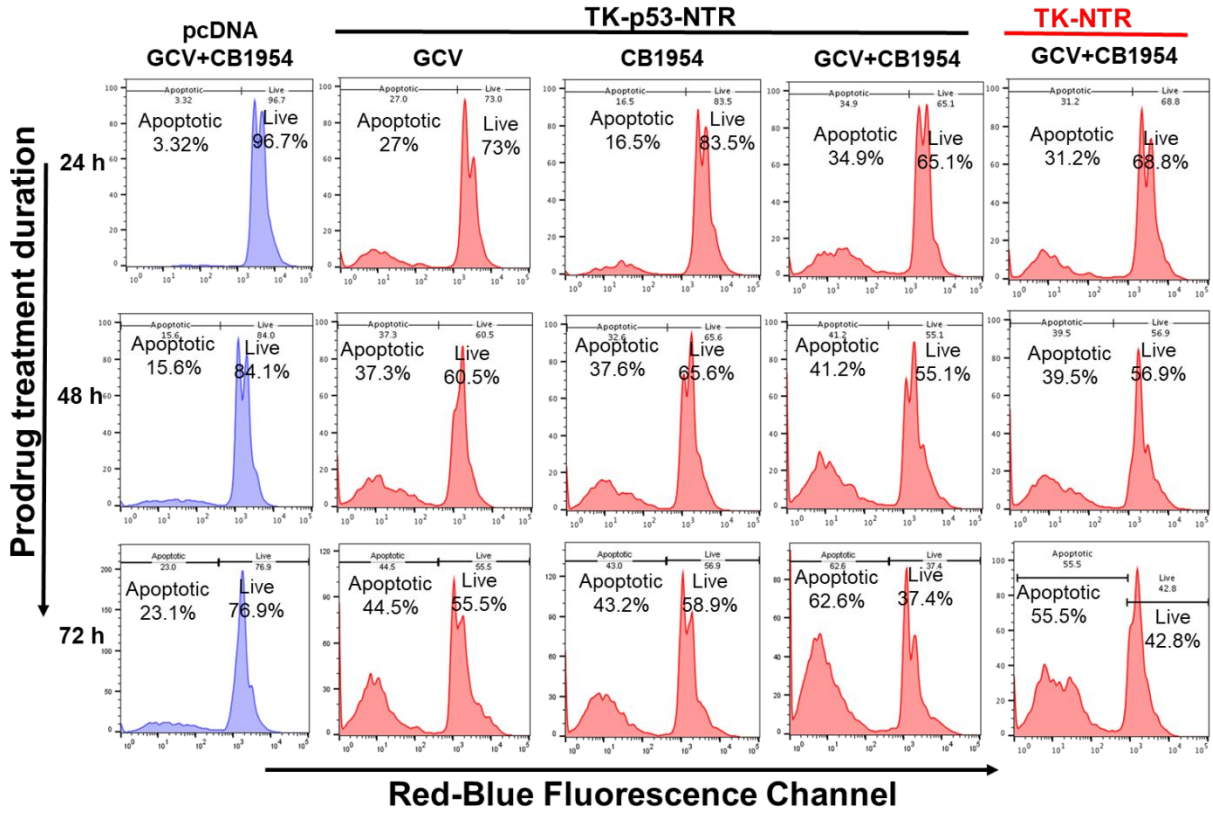

Fig. S11: TK-p53-NTR therapeutic efficacy in Hep3B Cells. PI staining-based flow cytometry assay measures apoptotic population at different time points (24 h, 48 h and 72 h) after Hep3B cells after delivered with pcDNA, or pcDNA-TK-NTR, or pcDNA-TK-p53-NTR by PLGA-PEG-PEI nanoparticles and treated with GCV and/or CB1954 prodrugs combination.

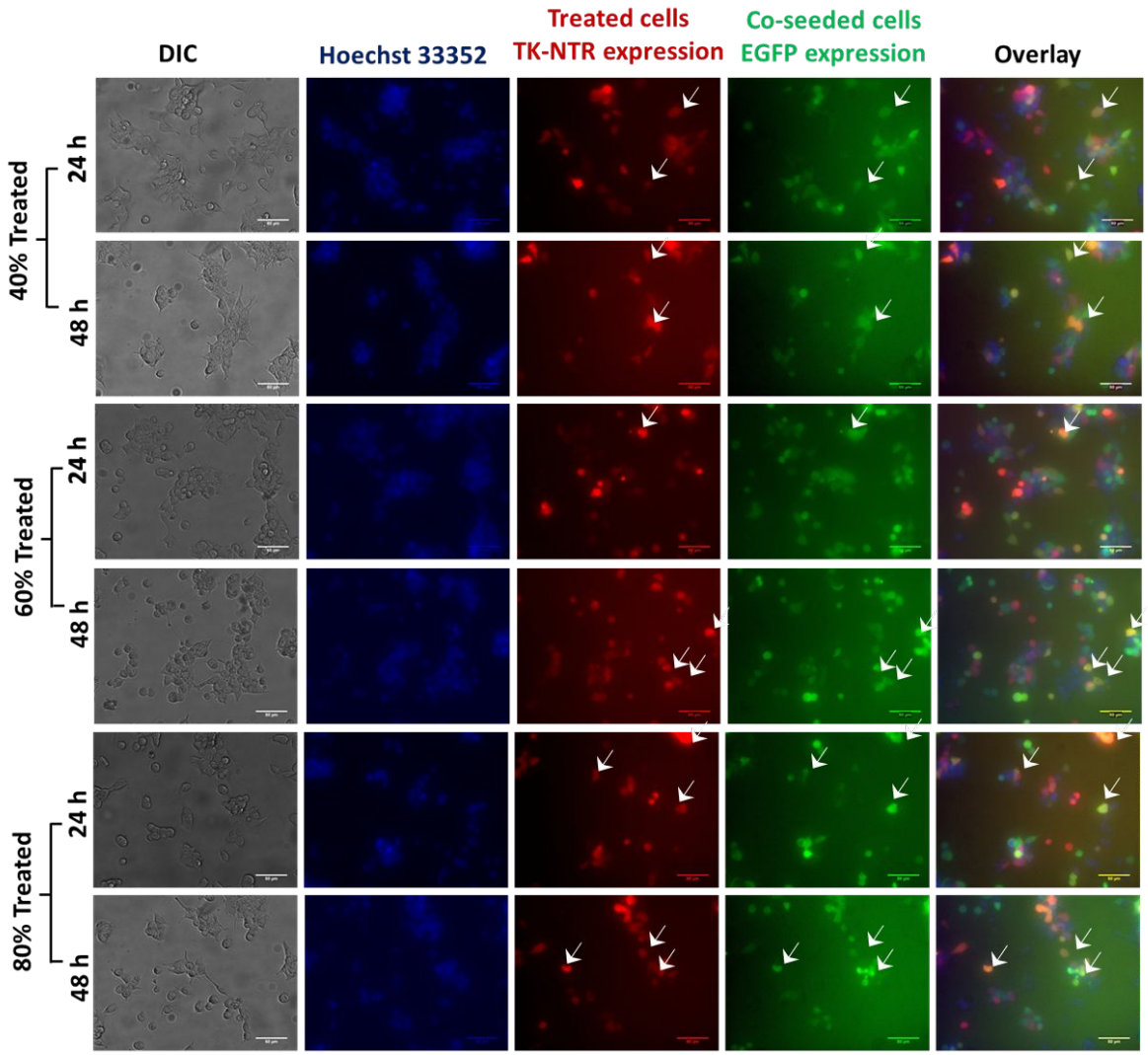

Fig. S12: Bystander effects of TK-p53-NTR; Evaluation of TK-p53-NTR bystander effects using fluorescence microscopy in co-culture of HepG2 cells stably expressing GFP (control cells) along with cells pretreated with TK-p53-NTR loaded PLGA-PEG-PEI nanoparticles in the presence of substrate CytoCy5S, imaged under DIC, DAPI (Hoechst 33342 nuclear stain), GFP (EGFP expression) and Cy5 (CytoCy5S) filters. Images obtained at 24 h and 48 h post treatment for different seeding combinations (40%, 60% and 80% treated cell populations). Arrows indicate the cells with both CytoCy5S and GFP colocalized signal as an indicator of bystander effect.

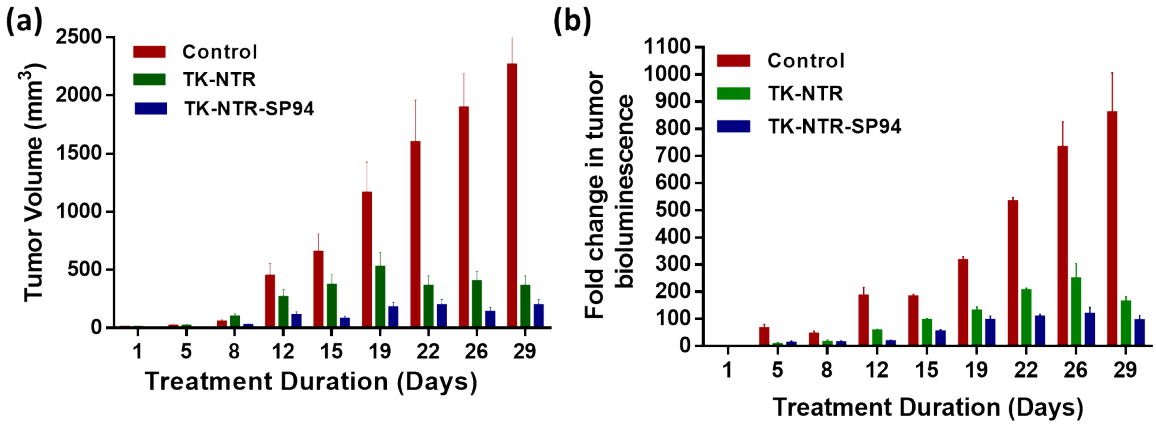

Fig. S13: Evaluation of TK-NTR therapeutic potential in HCC xenograft mice model; (a) representation of tumor growth volume at different time points as estimated by Vernier caliper measurements, and (b) the corresponding quantitative representation of the ROI bioluminescence values**.**

Supplementary Tables:

PLGA-PEG (mg)	PLGA-PEG (EDC/NHS) (mg)	L-PEI (mg)	Size (nm)	ζ Potential	PDI
5.0	5.0	1.0	165	+32.4	0.109
4.0	6.0	1.0	172	+38.3	0.243
6.0	4.0	1.0	147	+31.1	0.356

Table S1: Optimization of PEI conjugation on NP surface; Different ratios of PLGA-PEG with respect to the activated counterpart led to different extents of PEI grafting on the nanoparticle surface. This was reflected in the trend of size and ζ potential of the nanoparticles.

PLGA-PEG (wt%)	PLGA-PEG (EDC/NHS) (wt%)	PLGA-PEG-SP94 (wt%)	Size (nm)	PDI	ζ Potential
45%	45%	10%	174±15	0.234	+29.94
40%	40%	20%	173±37	0.274	+24.89
35%	35%	30%	177±84	0.386	+22.34

Table S2: Optimization of SP94 functionalization surface functionalization Different ratios of SP94 peptide conjugated PLGA-PEG incorporation into nanoparticles and their influence on the size and ζ potential of the nanoparticles.

References

1. Devulapally, R.; Sekar, N. M.; Sekar, T. V.; Foygel, K.; Massoud, T. F.; Willmann, J. K.; Paulmurugan, R., Polymer Nanoparticles Mediated Codelivery of Antimir-10b and Antimir-21 for Achieving Triple Negative Breast Cancer Therapy. *ACS Nano* **2015,** *9* (3), 2290-302.
2. McCall, R. L.; Sirianni, R. W., Plga Nanoparticles Formed by Single- or Double-Emulsion with Vitamin E-Tpgs. *J Vis Exp* **2013,** (82), 51015.
3. Mohammadian, F.; Abhari, A.; Dariushnejad, H.; Nikanfar, A.; Pilehvar-Soltanahmadi, Y.; Zarghami, N., Effects of Chrysin-Plga-Peg Nanoparticles on Proliferation and Gene Expression of Mirnas in Gastric Cancer Cell Line. *Iran J Cancer Prev* **2016,** *9* (4), e4190.
4. Wang, F.; Liu, P.; Nie, T.; Wei, H.; Cui, Z., Characterization of a Polyamine Microsphere and Its Adsorption for Protein. *Int J Mol Sci* **2012,** *14* (1), 17-29.
5. Yue, J.; Wu, J.; Liu, D.; Zhao, X.; Lu, W. W., Bmp2 Gene Delivery to Bone Mesenchymal Stem Cell by Chitosan-G-Pei Nonviral Vector. *Nanoscale Res Lett* **2015,** *10*, 203.
6. Alibolandi, M.; Ramezani, M.; Abnous, K.; Hadizadeh, F., As1411 Aptamer-Decorated Biodegradable Polyethylene Glycol-Poly(Lactic-Co-Glycolic Acid) Nanopolymersomes for the Targeted Delivery of Gemcitabine to Non-Small Cell Lung Cancer in Vitro. *J Pharm Sci* **2016,** *105* (5), 1741-1750.
7. Chen, X. A.; Zhang, L. J.; He, Z. J.; Wang, W. W.; Xu, B.; Zhong, Q.; Shuai, X. T.; Yang, L. Q.; Deng, Y. B., Plasmid-Encapsulated Polyethylene Glycol-Grafted Polyethylenimine Nanoparticles for Gene Delivery into Rat Mesenchymal Stem Cells. *Int J Nanomedicine* **2011,** *6*, 843-53.

8. Figueiredo, M.; Esenaliev, R., Plga Nanoparticles for Ultrasound-Mediated Gene Delivery to Solid Tumors. *J Drug Deliv* **2012,** *2012*, 767839.
9. Schmid, D.; Park, C. G.; Hartl, C. A.; Subedi, N.; Cartwright, A. N.; Puerto, R. B.; Zheng, Y.; Maiarana, J.; Freeman, G. J.; Wucherpfennig, K. W.; Irvine, D. J.; Goldberg, M. S., T Cell-Targeting Nanoparticles Focus Delivery of Immunotherapy to Improve Antitumor Immunity. *Nat Commun* **2017,** *8* (1), 1747.
10. Wu, C. H.; Lan, C. H.; Wu, K. L.; Wu, Y. M.; Jane, W. N.; Hsiao, M.; Wu, H. C., Hepatocellular Carcinoma-Targeted Nanoparticles for Cancer Therapy. *Int J Oncol* **2018,** *52* (2), 389-401.
11. Roacho-Perez, J. A.; Gallardo-Blanco, H. L.; Sanchez-Dominguez, M.; Garcia-Casillas, P. E.; Chapa-Gonzalez, C.; Sanchez-Dominguez, C. N., Nanoparticles for Deathinduced Gene Therapy in Cancer (Review). *Mol Med Rep* **2018,** *17* (1), 1413-1420.
12. Teng, G.; Ju, Y.; Yang, Y.; Hua, H.; Chi, J.; Mu, X., Combined Antitumor Activity of the Nitroreductase/Cb1954 Suicide Gene System and Gamma-Rays in Hela Cells in Vitro. *Mol Med Rep* **2016,** *14* (6), 5164-5170.
13. Sekar, T. V.; Foygel, K.; Ilovich, O.; Paulmurugan, R., Noninvasive Theranostic Imaging of Hsv1-Sr39tk-Ntr/Gcv-Cb1954 Dual-Prodrug Therapy in Metastatic Lung Lesions of Mda-Mb-231 Triple Negative Breast Cancer in Mice. *Theranostics* **2014,** *4* (5), 460-74.
14. Vaseva, A. V.; Moll, U. M., The Mitochondrial P53 Pathway. *Biochim Biophys Acta* **2009,** *1787* (5), 414-20.
15. Finucane, D. M.; Bossy-Wetzel, E.; Waterhouse, N. J.; Cotter, T. G.; Green, D. R., Bax-Induced Caspase Activation and Apoptosis Via Cytochrome C Release from Mitochondria Is Inhibitable by Bcl-Xl. *J Biol Chem* **1999,** *274* (4), 2225-33.
16. Zheng, T. S.; Schlosser, S. F.; Dao, T.; Hingorani, R.; Crispe, I. N.; Boyer, J. L.; Flavell, R. A., Caspase-3 Controls Both Cytoplasmic and Nuclear Events Associated with Fas-Mediated Apoptosis in Vivo. *Proc Natl Acad Sci U S A* **1998,** *95* (23), 13618-23.
17. Fujiwara, K.; Daido, S.; Yamamoto, A.; Kobayashi, R.; Yokoyama, T.; Aoki, H.; Iwado, E.; Shinojima, N.; Kondo, Y.; Kondo, S., Pivotal Role of the Cyclin-Dependent Kinase Inhibitor P21waf1/Cip1 in Apoptosis and Autophagy. *J Biol Chem* **2008,** *283* (1), 388-97.
18. Wu, J. M.; Sheng, H.; Saxena, R.; Skill, N. J.; Bhat-Nakshatri, P.; Yu, M.; Nakshatri, H.; Maluccio, M. A., Nf-Kappab Inhibition in Human Hepatocellular Carcinoma and Its Potential as Adjunct to Sorafenib Based Therapy. *Cancer Lett* **2009,** *278* (2), 145-155.